Applied Physics Letters

RESEARCH ARTICLE | JULY 08 2024

AlScN-on-SiC microelectromechanical Lamb wave resonators operating at high temperature up to 800 °C

Special Collection: (Ultra)Wide-bandgap Semiconductors for Extreme Environment Electronics

Wen Sui ; Philip X.-L. Feng

Appl. Phys. Lett. 125, 022201 (2024)
https://doi.org/10.1063/5.0185606

AIP Publishing

Applied Physics Letters ARTICLE pubs.aip.org/aip/apl

AlScN-on-SiC microelectromechanical Lamb wave resonators operating at high temperature up to 800 °C

Cite as: Appl. Phys. Lett. **125**, 022201 (2024); doi: 10.1063/5.0185606
Submitted: 31 October 2023 · Accepted: 19 June 2024 ·
Published Online: 8 July 2024

Wen Sui and Philip X.-L. Feng[a)]

AFFILIATIONS

Department of Electrical and Computer Engineering, Herbert Wertheim College of Engineering, University of Florida, Gainesville, Florida 32611, USA

Note: This paper is part of the APL Special Collection on (Ultra)Wide-bandgap Semiconductors for Extreme Environment Electronics.
[a)]**Author to whom correspondence should be addressed:** philip.feng@ufl.edu

ABSTRACT

We report on the experimental demonstration of aluminum scandium nitride (AlScN)-on-cubic silicon carbide (3C-SiC) Lamb wave resonators (LWRs) realized via microelectromechanical systems (MEMS) technology, operating at high temperature (T) up to $T = 800\,^{\circ}\mathrm{C}$, while retaining robust electromechanical resonances at ∼27 MHz and good quality factor of $Q \approx 900$ even at 800 °C. Measured resonances exhibit clear consistency and stability during heating and cooling processes, validating the AlScN-on-SiC LWRs can operate at high T up to 800 °C without noticeable degradation in moderate vacuum (∼20 mTorr). Even after undergoing four complete thermal cycles (heating from 23 to 800 °C and then cooling down to 23 °C), the devices exhibit robust resonance behavior, suggesting excellent stability and suitability for high-temperature applications. Q starts to decline as the temperature exceeds 400 °C, which can be attributed to energy dissipation mechanisms stemming from thermoelastic damping and intrinsic material loss originating from phonon–phonon interactions.

In the contemporary landscape of integrated systems, the effective functioning of various technologies is frequently challenged by thermal conditions that surpass the capabilities of existing robust or high-performance physical sensors. This necessitates a paradigm shift toward the development and utilization of microelectromechanical systems (MEMS) engineered specifically for high-temperature (high-T) and harsh-environment applications. The significance of this endeavor is underscored by its potential to usher in substantial reductions in size, weight, and power consumption (SWaP), which is critical and imperative across a multitude of strategic sectors. These sectors, which include but are not limited to automotive, aerospace, turbomachinery, oil well/logging equipment, industrial process control, nuclear power, and defense communications, demand robust and seamless operations of MEMS in extreme conditions.[1–4] In the automotive and aerospace industries, conventional systems operate within a temperature range spanning from 20 to 600 °C. This wide thermal spectrum is a testament to the diversity of challenges faced by these sectors, encompassing everything from the frigid conditions of high-altitude flight to the scorching heat generated within internal combustion engines. However, it is in environments of unparalleled extremity, such as those found in gas turbine engines and nuclear power generators, where MEMS for high-T and harsh-environment applications truly proves their mettle. Here, temperatures can soar beyond the 900 °C mark, pushing the boundaries of conventional sensor technologies.[5,6] Thus, MEMS must be meticulously designed and operated, accounting for reduced performance and engineering margins to mitigate risks in high-T and hostile environments.[7–9]

Developing devices for high-T applications presents two central challenges: selecting suitable materials and creating robust interfaces.[10,11] The quest for suitable materials in high-T applications transcends the mere pursuit of high melting points. Equally crucial is the preservation of material performance even under the most extreme thermal conditions. The material should resist degradation as temperatures surge, ensuring that the MEMS devices function reliably and predictably. The challenge of interfacing arises from three key sources: (i) ensuring efficient power and signal transfer within a high-T environment, (ii) selecting suitable materials for interfaces, such as tubing and contacts, guided by the same stringent criteria as those governing the

core material choice, and (iii) addressing thermomechanical effects. These effects, including mismatches in thermal expansions among different materials and the resultant residual stresses, have the potential to significantly impact device operation. Achieving a robust design and conducting accurate simulations hinge on a comprehensive understanding of how key parameters, such as device geometry, material density, and Young's modulus, respond to temperature variations.

Aluminum nitride (AlN) offers significant potential for high tolerance to extreme environmental conditions.[12,13] To date, the highest operating temperature of AlN based MEMS resonators has been reported up to 700 °C.[14] AlN has demonstrated the retention of its piezoelectric properties at temperatures up to 1150 °C.[15] The incorporation of scandium (Sc) into AlN leads to a remarkable enhancement in the piezoelectric coefficient.[16,17] These enduring high-performance attributes position AlScN as a highly promising candidate for sensor applications in extreme high-T environments.[18–21] Figure 1 summarizes the potential technical rationales and main physical effects to probe on AlScN-on-Silicon carbide (SiC) MEMS for high-T applications. Earlier, we have demonstrated AlScN-on-cubic silicon carbide (3C-SiC) heterostructure diaphragm optomechanical resonant transducers (no metallization) capable of operating in high-T environment up to 600 °C.[22] However, the previous devices operate without metal electrodes, relying on all-optical drive and detection. The current work is focused on investigating and demonstrating high-temperature capabilities of AlScN-on-SiC stack with electrodes for all-electrical transducers. In this Letter, we report on the experimental demonstration of AlScN-on-SiC MEMS Lamb wave resonators (LWRs) operating at high temperatures up to 800 °C.

Single-crystal n-type 3C-SiC (100) thin film with the thickness of 900 nm is grown on Si(100) substrate by the low pressure chemical vapor deposition (LPCVD) process. 1 μm-Thick AlScN with 20% Sc is then sputtered on top of the 3C-SiC epilayer on Si substrate. Figure 2(a) shows the X-ray diffraction (XRD) analysis of the AlScN/3C-SiC heterostructure on Si obtained in the conventional θ–2θ scan mode. We observe the peaks corresponding to the (100) plane for the SiC layer, which indicates that single-crystal 3C-SiC(100) is grown on Si (100). Three peaks are observed for AlScN, which confirms the polycrystalline nature with the preferred orientation along the c-axis, i.e., AlScN (002) peak. A well-defined and narrow rocking curve for 3C-SiC (200) peak indicates that the SiC layer is well-aligned with the Si substrate and has a high degree of crystalline perfection [Fig. 2(b)]. The rocking curve for the AlScN (002) peak indicates high crystalline quality and a strong preferred orientation along the c-axis, suggesting that the AlScN layer is predominantly oriented in the (002) plane [Fig. 2(c)]. The full width at half maximum (FWHM) is 0.62° for the SiC (200) peak and 2.09° for the AlScN (002) peak. Figure 2(d) shows the transmission electron microscopy (TEM) image of the cross-sectional AlScN/SiC interface, which clearly displays the columnar growth of AlScN film. Grain boundaries are not observed in the 3C-SiC thin film, while the main defects are stacking faults well known in 3C-SiC grown on Si.[23,24] The selected area electron diffraction (SAED) pattern as shown in Figs. 2(e) and 2(f) reinforces the XRD results and confirms that the 3C-SiC layer is single-crystalline, and the AlScN thin film is polycrystalline.

The resonance center frequency of the Lamb wave resonator can be expressed as[25]

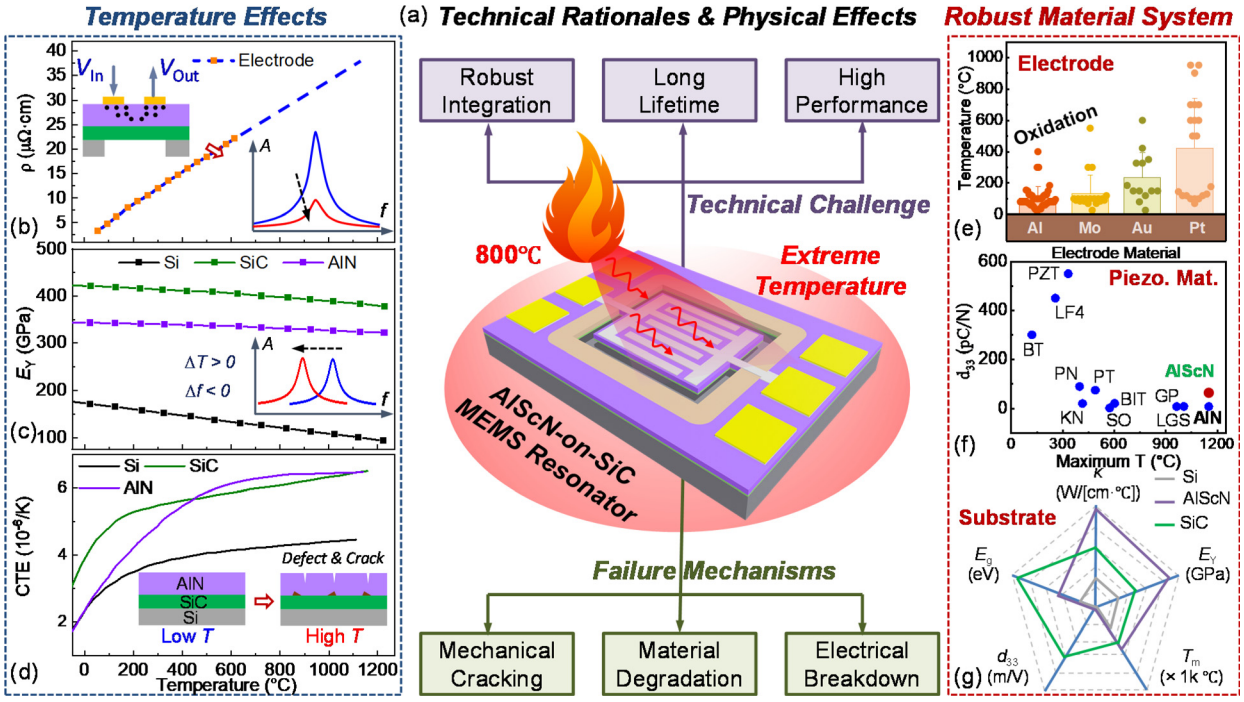

FIG. 1. Scientific background of MEMS for high-T applications. (a) Technical rationales and main intriguing physical effects to probe and understand on the AlScN-on-SiC platform. Temperature effects on (b) resistivity of metal electrode, (c) Young's modulus (E_Y), and (d) coefficient of thermal expansion (CTE). Robust material selection, including (e) metal material for electrodes, (f) piezoelectric materials, and (g) structural materials.

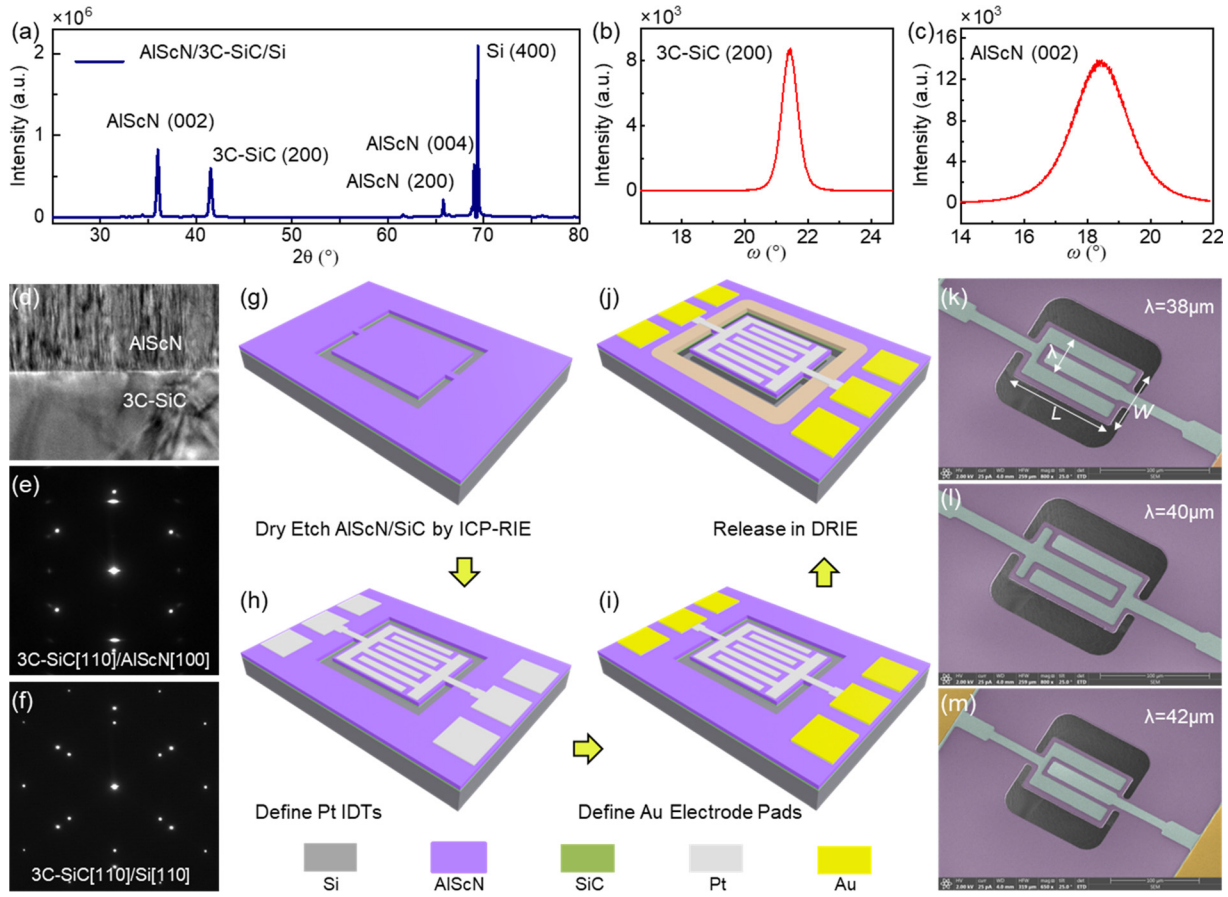

FIG. 2. (a) XRD analysis of the AlScN/3C-SiC heterostructure on Si. (b) and (c) Rocking curves of 3C-SiC (200) peak and AlScN (002) peak. (d) TEM cross-sectional image of the AlScN/3C-SiC interface. SAED patterns of (e) 3C-SiC[110]/Si[110] and (f) 3C-SiC/AlScN in the [110] orientation. Schematic illustration of fabrication process of the AlScN/SiC LWRs. (g) Dry etch AlScN and SiC in sequence by ICP RIE. (h) Pattern and sputter 100 nm Pt as IDTs with 10 nm Ti as the adhesion layer, and lift off. (i) Pattern and sputter 500 nm Au electrode pads and lift off. (j) Release the resonant body by carefully dry etching Si in DRIE. SEM images of devices with (k) $\lambda = 38$ μm, (l) $\lambda = 40$ μm, and (m) $\lambda = 42$ μm.

$$f_0 = \frac{v_p}{\lambda}, \tag{1}$$

where λ is the wavelength and V_p represents the acoustic wave velocity. The acoustic wave velocity of the lowest order antisymmetric mode (A_0 mode) is related to the thickness of the thin plate,[25]

$$v_p = \frac{2\pi h}{\lambda}\sqrt{\frac{E_Y}{12(1-\nu^2)\rho}}\frac{1}{\sqrt{\frac{\pi^2 h^2}{3\lambda^2}+1}}, \tag{2}$$

where h is the thickness of the plate, E_Y represents Young's modulus, ν is the Poisson ratio, and ρ is the mass density. The A_0 mode (flexural plate mode) of the LWRs is designed to operate in 20–30 MHz range with λ changes from 38 to 42 μm.

The AlScN LWR is built using a 4-mask fabrication process. First, a chromium (Cr) etch mask is sputtered and patterned for the subsequent dry etching of 1 μm AlScN thin film and 0.9 μm SiC thin film in chlorine (Cl_2) based and sulfur hexafluoride (SF_6) based inductively coupled plasma reactive ion etching (ICP-RIE), respectively, to define the shape of the suspended AlScN/SiC resonant body [Fig. 2(g)]. Following the dry etching, the Cr hard mask is removed by wet etching. 100 nm platinum (Pt) is then sputtered with 10 nm titanium (Ti) as the adhesion layer and patterned by the 2nd photolithography as the interdigital transducers (IDTs) [Fig. 2(h)]. After that, 500 nm gold (Au) electrode pads are defined by the photolithography #3 and a sputtering and liftoff process [Fig. 2(i)]. Next, the devices are released via a deep reactive ion etch (DRIE) of the Si substrate with photoresist as the mask for protecting the metallization layer [Fig. 2(j)]. Finally, the photoresist is removed gently by oxygen (O_2) plasma. Figures 2(k)–2(m) show the scanning electron microscopy (SEM) images of three LWRs with λ equals to 38, 40, and 42 μm, respectively.

There are several commonly used methods to heat MEMS devices and perform high-T measurements, such as silicon hotplate, Peltier stage, hot air gun, infrared (IR) lamp, resistive heater, and tubular furnace.[26–28] The selection of the heating method primarily depends on

the specific requirements of the study. The size and geometry of the MEMS device, the temperature range that needs to be covered, and the desired level of temperature control are some of the key factors to consider when choosing the heating method. The aforementioned methods suffer from a lack of integration and are limited in their capacity to deliver extremely high temperatures and precise temperature measurements. Here, we customize a ceramic heater type of micro-probe system for extremely high-T testing, as shown in Fig. 3(a), a subminiature probe system with vacuum and temperature control functions. The equipment is capable of measuring the electrical properties of MEMS in the temperature range of room temperature to 1000 °C. To perform the resonance frequency measurements, the sample was mounted on the ceramic heater and heated to the desired temperature. The temperature was monitored and controlled using the built-in temperature control functions of the equipment. Once the sample reached the desired temperature, the resonance frequency of the sample was measured using a network analyzer (HP3577A). The network analyzer's output port drives the resonator with a radio-frequency (RF) voltage v_{in} (input to the device), with sweeping frequency but with amplitude set at 150 mV root mean square (rms) for all measurements. The response from the resonator in voltage signal, v_{out} (output from the device), is measured at the input port of the network analyzer. The data plots of amplitude of v_{out} vs frequency demonstrate the device's resonance responses in the voltage domain, as shown in Figs. 4(d)–4(e) and 5(a)–5(c). Details of the measurement scheme are provided in the supplementary material. To ensure accurate measurements, the sample was allowed to stabilize at the desired temperature for a sufficient period before taking the resonance frequency measurement. Figure 3(b) shows the temperature regulation in both heating and cooling with the temperature ranging from room temperature to 800 °C. At each temperature point, we wait ∼10 min for the temperature to stabilize and then take the resonance measurements. The inset shows the chip under test at 800 °C.

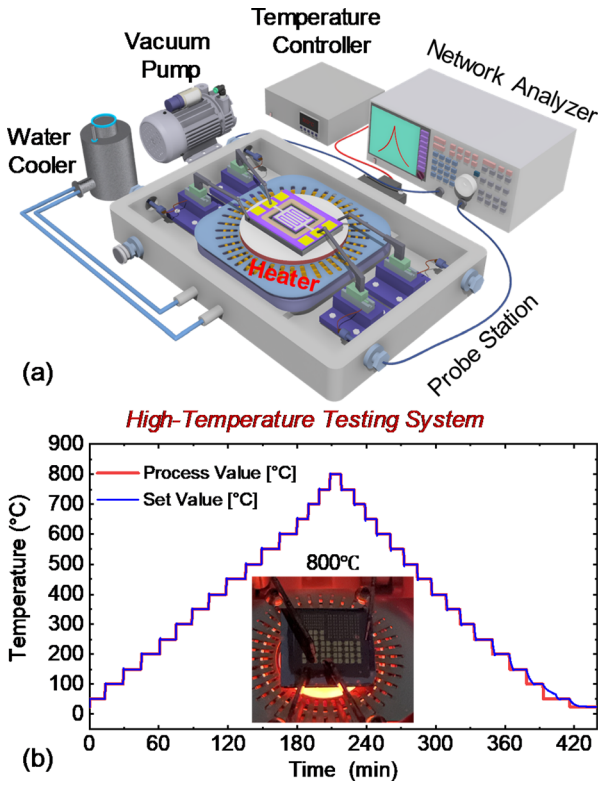

FIG. 3. (a) Illustration of the high-T electrical probing system for testing devices. (b) Temperature regulation from 23 to 800 °C (heating up to 800 °C and cooling back to 23 °C). The inset shows a photograph of a chip under test at 800 °C.

We first measure the resonance of an AlScN LWR with $\lambda = 38\,\mu m$ in 20 mTorr vacuum at room temperature. As shown in Fig. 4(a), we observe a resonance mode at ∼27 MHz. Figure 4(b) shows the equivalent circuit model of the device. The simulated resonance agrees well with the measurement. Figure 4(c) displays the mode shape of the measured A_0 mode simulated in COMSOL. The T-dependent resonance responses of a AlScN LWR with $\lambda = 38\,\mu m$ measured in both heating and cooling processes are illustrated in Figs. 4(d) and 4(e), respectively. The resonance gradually downshifts from 27.1947 to 26.8569 MHz as the temperature increases from room temperature up to 800 °C. Even at these elevated temperatures, the device remarkably maintains its robust resonance behavior, sustaining a resonant frequency at ∼27 MHz with a conspicuously sharp peak. We then gradually decrease the temperature back to room temperature. As expected, the resonance gradually upshifts in the cooling process. We observe clear consistency in resonances measured during heating and cooling, validating the AlScN-on-SiC MEMS LWR can operate reliably at high temperatures up to 800 °C without noticeable degradation.

Intriguingly, an elevation in the baseline of the resonance curve is observed with increasing temperature. The increased capacitive feedthrough with increasing temperature is similar to the rising background response with increasing RF drive while at stabilized room temperature, and may come from several aspects. First, higher temperatures can increase the leakage currents through the device heterostructure, which can lead to changes in the effective impedance and impact the RF feedthrough. Second, the dielectric constant of AlScN-on-SiC stack may increase with temperature, resulting in a larger capacitance. Third, the difference in the thermal expansion of metal and AlScN-on-SiC stack may change the gaps between IDTs, leading to the change of the effective impedance. To decouple from the background response and gain a clear and more nuanced understanding of the temperature-dependent resonance, we subtracted the background from the resonance curves measured at each temperature in both heating and cooling processes, as shown in Figs. 4(f) and 4(g). The procedures for the linear background (baseline) removal and system calibration results at varying temperatures are detailed in the supplementary material. The background-removed resonance curves reveal a slight attenuation in the resonance amplitude as the temperature rises, suggesting energy losses at elevated temperatures. Remarkably, this phenomenon exhibits a harmonious consistency in both heating and cooling processes, with the amplitude gradually recovering as the temperature descends from 800 to 23 °C. These findings collectively underscore the exceptional performance and resilience of the AlScN-on-SiC MEMS LWR, affirming its capacity to operate reliably under the extreme thermal conditions of up to 800 °C while unraveling intriguing temperature-dependent behavior.

To assess the resilience of AlScN-on-SiC MEMS LWRs under extreme temperatures, we conducted resonance measurements on three additional devices located on the same chip, subjecting them to

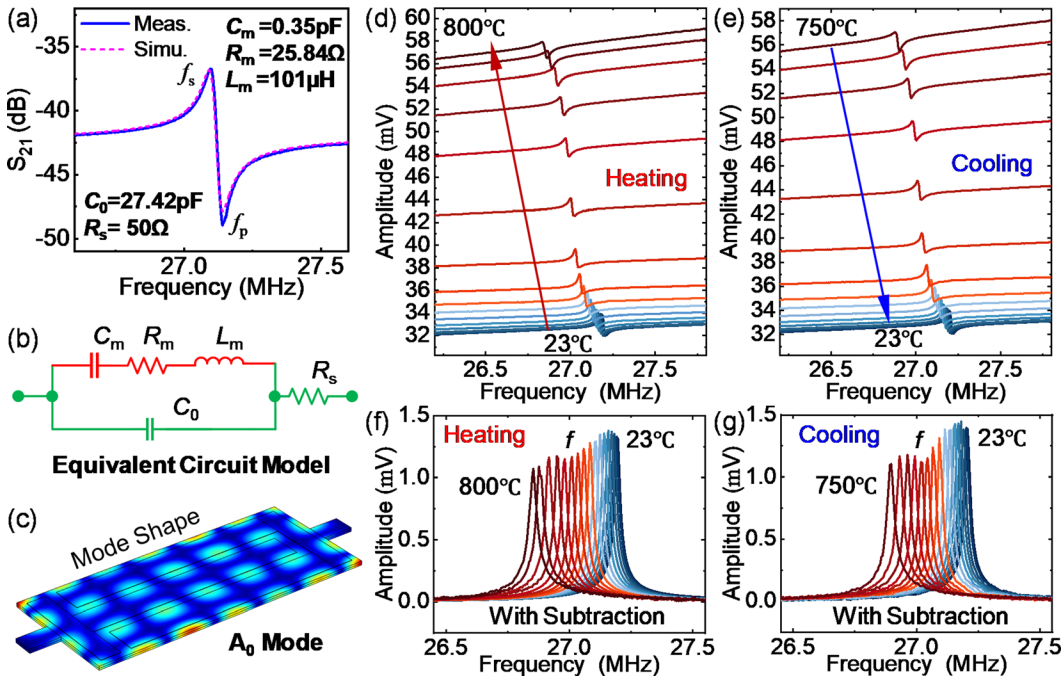

FIG. 4. (a) Resonance of an AlScN-on-SiC LWR with $\lambda = 38\,\mu m$ measured at room temperature in 20 mTorr vacuum. f_s represents series resonance and f_p represents parallel resonance. The magenta dashed line shows simulated data with the equivalent circuit parameters. (b) Equivalent circuit model, with R_m, L_m, and C_m representing motional resistance, inductance, and capacitance, respectively. C_0 is the static capacitance, and R_s is used to model the parasitic Ohmic loss of the electrode. (c) Mode shape of the A_0 mode. Temperature-dependent resonance responses of the AlScN-on-SiC LWR measured in (d) heating and (e) cooling cycles, with the background-subtracted resonance curves shown in (f) and (g), respectively.

both heating and cooling cycles in the temperature range from room temperature to 800 °C. Figure 5 shows the temperature effects on the resonance for the devices tested in the 2nd, 3rd, and 4th thermal cycles. Figures 5(a)–5(c) show the resonance curves before and after background subtraction for devices with $\lambda = 42\,\mu m$, $\lambda = 38\,\mu m$, and $\lambda = 40\,\mu m$, respectively, measured at room temperature. All the other resonance curves are shown in the supplementary material. We observe great consistency in resonances (including f_s and f_p obtained from raw data, and the center peak frequency f extracted from the background-subtracted resonance curves) measured during heating and cooling cycles for all three devices, as depicted in Figs. 5(d)–5(f). Notably, even after undergoing four complete thermal cycles, the device exhibits robust resonance behavior, underscoring its exceptional stability and suitability for high-T applications. To gain deeper insights into the frequency response to temperature, we have examined the frequency shift at different temperatures with respect to its resonance frequency at room temperature for each device in Figs. 5(g)–5(i). Three devices present similar frequency response patterns, characterized by three distinct linear segments of fractional frequency downshift within the measured temperature range. At lower temperatures, below 250 °C, the average temperature coefficient of resonance frequency (TCf) of the three devices is calculated to be about −9 ppm/°C, which is about half of that measured in higher temperature region of 250–500 °C, where the average TCf measures around −17 ppm/°C. A larger TCf is obtained when the temperature exceeds 500 °C, with the average TCf ranging between −23 and −28 ppm/°C. To get insight into the evolution of TCf with temperature, we calculate the TCf at each temperature point by using the resonance frequencies measured at two adjacent temperatures, as shown in Figs. 5(j)–5(l). A linear increase in absolute TCf values from about 10 to 29 ppm/°C is observed as the temperature increases up to 750 °C. Interestingly, a turnover point occurs in the TCf plot for all the three devices at ∼800 °C, which may result from the thermal instability caused by the change of stress distribution inside the heterostructure.[22]

Figures 5(m)–5(o) present the Q as a function of temperature for both the heating and cooling processes. Q shows slight changes when T is below 400 °C, while a consistent degradation in Q with increasing temperature is observed when T is above 400 °C. Rapid material property changes throughout the wide operation temperature range will lead to a complicated situation for the temperature dependence of the Q. There are various possible energy loss mechanisms that can reduce the Q of MEMS resonators, such as air-damping, thermoelastic dissipation, anchor loss, and other situations shown in the following equation:

$$\frac{1}{Q_{\text{Total}}} = \frac{1}{Q_{\text{Air}}} + \frac{1}{Q_{\text{TED}}} + \frac{1}{Q_{\text{Anchor loss}}} + \frac{1}{Q_{\text{Others}}}. \tag{3}$$

Here, we ignore the Q_{Air} and $Q_{\text{Anchor loss}}$ terms because the measurements are all done in vacuum where air damping is largely eliminated, and the anchor loss usually has a negligible temperature dependence.[29] The temperature dependence of Q_{TED} can be expressed as[30]

$$Q_{\text{TED}} = Q_{\text{TED,freq}} Q_{\text{TED,mat}} = \frac{f_{M+}^2 f_T^2}{f_M f_T} \frac{C_p \rho}{\alpha^2 T E_Y}, \tag{4}$$

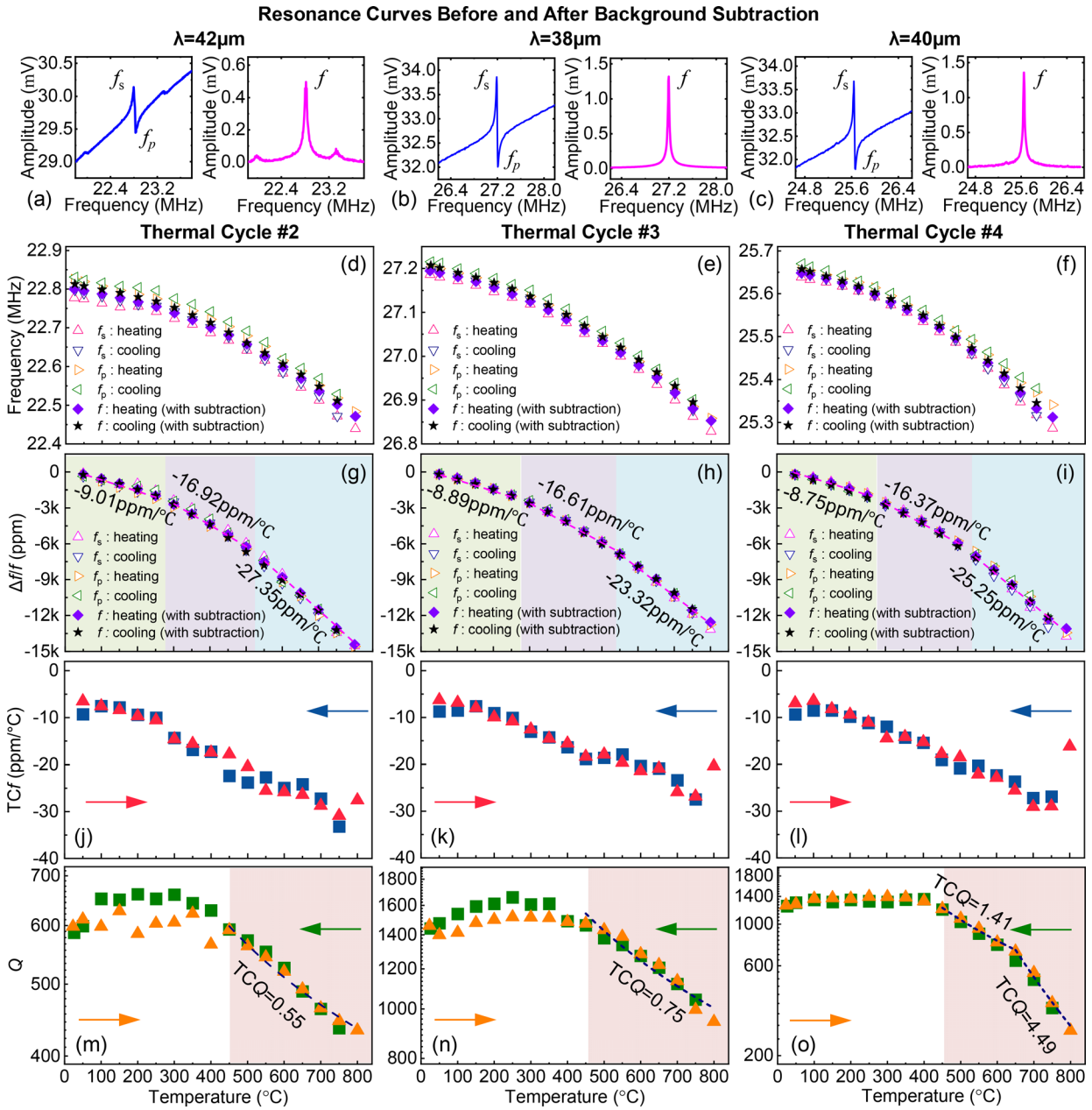

FIG. 5. Resonance curves before and after background subtraction for devices with (a) $\lambda = 42\,\mu m$, (b) $\lambda = 38\,\mu m$, and (c) $\lambda = 40\,\mu m$ measured at room temperature. Measured temperature-dependent resonance frequencies [f_s, f_p, and f as illustrated in panels (a)–(c)] for devices with (d) $\lambda = 42\,\mu m$, (e) $\lambda = 38\,\mu m$, and (f) $\lambda = 40\,\mu m$, respectively, in both heating and cooling processes. f_s and f_p values are obtained from raw data without background subtraction, while f values are extracted from background-subtracted resonance curves. The corresponding fractional frequency shift ($\Delta f/f_0$) with varying temperature plots for f_s, f_p, and f is shown in (g)–(i). f_0 is the frequency measured at room temperature. The averaged TCf is obtained by linear fitting of the $\Delta f/f_0$ vs temperature. (j)–(l) TCf vs temperature, where the TCf at different temperatures is calculated by $TCf(T) = (1/f(T)) \times (\Delta f/\Delta T)$. (m)–(o) Measured Q as a function of temperature for both the heating and cooling processes.

where $Q_{TED,freq} = \frac{f_M^2 + f_T^2}{f_M f_T}$ is the frequency term and $Q_{TED,mat} = \frac{C_p \rho}{\alpha^2 T E_Y}$ is related to the material properties. Here, C_p represents specific heat capacity, ρ is the mass density, α is the thermal expansion coefficient, and E_Y is the Young's modulus. f_M is the mechanical mode frequency, and f_T is the thermal mode frequency, which is the inverse of the thermal decay time, τ of the heat flow across the device. $Q_{TED,mat}$ demonstrates a pronounced decline with rising temperatures since it is solely contingent on material parameters. However, the temperature dependency of $Q_{TED,freq}$ is determined by the relationship of f_M and f_T. Specifically, $Q_{TED,freq}$ will decrease with the temperature increases if

$f_T > f_M$ at the original temperature. Conversely, $Q_{TED,freq}$ will increase as increasing the temperature if $f_T < f_M$ at the original temperature. For a specific f_M, the Q_{TED} value reaches the minimum when f_T is close to f_M due to the increased thermomechanical coupling. Below 400 °C, we observe subtle variations in Q, likely arising from the interplay between $Q_{TED,freq}$ and $Q_{TED,mat}$. Q shows a slight upward trend with temperature, attributed to the gradual increase in $Q_{TED,freq}$, while material properties remain relatively stable below 400 °C, resulting in a comparatively minor decrease in $Q_{TED,mat}$. However, as the temperature exceeds 400 °C, the influence of $Q_{TED,mat}$ becomes predominant, leading to a rapid decline in Q with increasing temperature. Note that after four thermal cycles, the Q shows better consistency in heating and cooling phases, which may be attributed to the enhanced crystallinity and reduced defects achieved through the annealing process. For better understanding, we fit the Q plot and extract the temperature coefficient of quality factor (TCQ),

$$Q \propto \frac{1}{T^{\beta}}, \tag{5}$$

where the exponential β is defined as the TCQ (TC$Q = \beta$). The results indicate that the TCQ value increases from 0.55 to 4.49 with prolonged exposure of the chip to multiple thermal cycles, signifying a swifter decline in Q as the temperature rises. Remarkably, even after four thermal cycles, Q exhibits a noteworthy capacity for recovery to its original values at room temperature.

In conclusion, we have demonstrated AlScN-on-SiC MEMS LWRs operating at high temperatures up to 800 °C. These LWRs maintain robust resonances and sustain good Qs of ~900 even at 800 °C. Both the resonances and Qs display consistency and stability during both heating and cooling processes. The devices persevere with reliable resonance behavior even after undergoing four complete thermal cycles (heating from 23 to 800 °C and then cooling down to 23 °C), highlighting its suitability for demanding high-T applications. Q remains nearly constant when the temperature is below 400 °C, while it starts to decline linearly with further elevation of the temperature. TCQ value increases from 0.55 to 4.49 with prolonged exposure of the devices to multiple thermal cycles, which represents a faster decline in Q as temperature rises. The temperature dependency of Q can be attributed to energy dissipation mechanisms stemming from thermoelastic damping. This study paves the way for advancing AlScN-on-SiC MEMS transducers into high-T and hostile environments.

See the supplementary material for resonance measurement scheme, calibration of background response (no resonator) with varying temperature, procedure for subtraction of linear background and extraction of quality (Q) factor, and temperature-dependent resonances of AlScN-on-SiC Lamb wave resonators (LWRs).

We thank the financial support from the National Science Foundation (NSF) ECCS EAGER Program (Grant No. ECCS-2221881) and Air Force Office of Scientific Research (AFOSR) Basic Research Program (Grant No. FA9550-23-1-0304).

AUTHOR DECLARATIONS

Conflict of Interest

The authors have no conflicts to disclose.

Author Contributions

Wen Sui: Conceptualization (equal); Data curation (lead); Investigation (lead); Methodology (equal); Validation (lead); Visualization (lead); Writing – original draft (lead); Writing – review & editing (equal). **Philip X.-L. Feng:** Conceptualization (lead); Data curation (supporting); Funding acquisition (lead); Investigation (equal); Methodology (equal); Project administration (lead); Resources (lead); Supervision (lead); Validation (equal); Visualization (supporting); Writing – original draft (supporting); Writing – review & editing (equal).

DATA AVAILABILITY

The data that support the findings of this study are available within the article and its supplementary material.

REFERENCES

[1]C. Wu, X. Fang, Q. Kang, Z. Fang, J. Wu, H. He, D. Zhang, L. Zhao, B. Tian, and R. Maeda, Microsyst. Nanoeng. **9**, 41 (2023).
[2]W. A. Gill, I. Howard, I. Mazhar, and K. McKee, Sensors **22**, 7405 (2022).
[3]C. Acar, A. R. Schofield, A. A. Trusov, L. E. Costlow, and A. M. Shkel, IEEE Sens. J. **9**, 1895–1906 (2009).
[4]W. Sui, S. M. E. H. Yousuf, Y. Liu, S. J. Pearton, and P. X.-L. Feng, Adv. Mater. Technol. **9**, 2301356 (2024).
[5]M. K. Dounkal, R. K. Bhan, and N. Kumar, Microsyst. Technol. **26**, 377–394 (2019).
[6]J. Han, P. Cheng, H. Wang, C. Zhang, J. Zhang, Y. Wang, L. Duan, and G. Ding, Mater. Lett. **125**, 224–226 (2014).
[7]P. Mahanta, F. Anwar, and R. Coutu, Sensors **19**, 579 (2019).
[8]W. Dong, S. Liu, S. J. Bae, and Y. Cao, Reliab. Eng. Syst. Saf. **205**, 107260 (2021).
[9]M. Hommel, H. Knab, and S. G. Yousef, Microelectron. Reliab. **126**, 114252 (2021).
[10]L. Wang, H. Liu, and X. Liu, Micromachines **13**, 743 (2022).
[11]W. Sui, T. Kaisar, H. Wang, Y. Wu, J. Lee, H. Xie, and P. X.-L. Feng, IEEE Sens. J. **24**, 7273–7283 (2024).
[12]W. Sui, X.-Q. Zheng, J. T. Lin, J. Lee, J. L. Davidson, R. A. Reed, R. D. Schrimpf, B. W. Alphenaar, M. L. Alles, and P. X.-L. Feng, IEEE Trans. Nucl. Sci. **69**, 216–224 (2022).
[13]A. Qamar, S. R. Eisner, D. G. Senesky, and M. Rais-Zadeh, J. Microelectromech. Syst. **29**, 900–905 (2020).
[14]C. M. Lin, T. T. Yen, V. V. Felmetsger, and A. P. Pisano, Appl. Phys. Lett. **97**, 083501 (2010).
[15]W. Sui, X.-Q. Zheng, J. T. Lin, B. W. Alphenaar, and P. X.-L. Feng, J. Microelectromech. Syst. **30**, 521–529 (2021).
[16]O. Zywitzki, T. Modes, S. Barth, H. Bartzsch, and P. Frach, Surf. Coat. Technol. **309**, 417–422 (2017).
[17]M. Park, Z. Hao, R. Dargis, A. Clark, and A. Ansari, J. Microelectromech. Syst. **29**, 490–498 (2020).
[18]M. R. Islam, N. Wolff, M. Yassine, G. Schönweger, B. Christian, H. Kohlstedt, O. Ambacher, F. Lofink, L. Kienle, and S. Fichtner, Appl. Phys. Lett. **118**, 232905 (2021).
[19]D. Drury, K. Yazawa, A. Zakutayev, B. Hanrahan, and G. Brennecka, Micromachines **13**, 887 (2022).
[20]J. Wang, M. Park, and A. Ansari, J. Microelectromech. Syst. **31**, 234–240 (2022).
[21]N. Wolff, M. R. Islam, L. Kirste, S. Fichtner, F. Lofink, A. Žukauskaitė, and L. Kienle, Micromachines **13**, 1282 (2022).
[22]W. Sui, H. Wang, J. Lee, A. Qamar, M. Rais-Zadeh, and P. X.-L. Feng, Adv. Funct. Mater. **32**, 2202204 (2022).
[23]H. Nagasawa, K. Yagi, T. Kawahara, and N. Hatta, Chem. Vap. Deposition **12**, 502–508 (2006).
[24]F. L. Via, A. Severino, R. Anzalone, C. Bongiorno, G. Litrico, M. Mauceri, M. Schoeler, P. Schuh, and P. Wellmann, Mater. Sci. Semicond. Process. **78**, 57–68 (2018).

[25]M. Liu, J. Li, J. Ma, and C. Wang, J. Semicond. **32**, 044006 (2011).
[26]E. J. Boyd, L. Li, R. Blue, and D. Uttamchandani, Sens. Actuator A: Phys. **198**, 75–80 (2013).
[27]M. Pozzi, M. Hassan, A. J. Harris, J. S. Burdess, L. Jiang, K. K. Lee, R. Cheung, G. J. Phelps, N. G. Wright, and C. A. Zorman, J. Phys. D: Appl. Phys. **40**, 3335 (2007).
[28]T. Aubert, J. Bardong, O. Legrani, O. Elmazria, M. Badreddine Assouar, G. Bruckner, and A. Talbi, J. Appl. Phys. **114**, 014505 (2013).
[29]S. Fei and H. Ren, Micromachines **12**, 143 (2021).
[30]B. Kim, M. A. Hopcroft, R. N. Candler, C. M. Jha, M. Agarwal, R. Melamud, S. A. Chandorkar, G. Yama, and T. W. Kenny, J. Microelectromech. Syst. **17**, 755–766 (2008).